



Flow Structure Investigation of a Truck under Crosswinds

J. Levin[†] and S. H. Chen

Department of Aeronautics and Astronautics, National Cheng Kung University, Tainan City, 701, Republic of China

[†]Corresponding Author Email: p48067049@gs.ncku.edu.tw

(Received January 9, 2022; accepted May 30, 2022)

ABSTRACT

This paper investigates the flow structures on the near- and far-wake of a 1/8th scaled simplified heavy vehicle model called Ground Transportation System (GTS) model using a steady-state Reynolds-averaged Navier-Stokes (RANS) with $k-\omega$ Shear Stress Transport (SST) turbulence model at Reynolds number (Re) of 1.6×10^6 and yaw angles (Ψ) = 0° - 14° . The current CFD results have been validated using experimental data from the literature. Two crosswind conditions based on the crosswind incidence angle (β) are adopted; $\beta < 90^\circ$ is called *crosswind*, and $\beta = 90^\circ$ (perpendicular to the GTS side surface) is called *pure crosswind*. Vortex detection scheme based on Ω method and total pressure coefficient (C_{pt}) contours is used to visualize the wake structure. With Ψ , vortices on the GTS roof take birth as a result of pressure differences between the windward and leeward sides. These vortices grow in size as they travel downstream. The growth in size is related to the Helmholtz theorem of vorticity and Kelvin's Circulation Theorem. The vortices merged at $Z/W > -4$ ($Z/W = 0$ is the GTS rear surface) downstream of the GTS for $\Psi = 7.5^\circ$ and 14° . The merged vortex dissipates at $Z/W > -6$ and $Z/W > -8$ for $\Psi = 7.5^\circ$ and 14° , respectively. In the *pure crosswind* condition, the merged vortex attaches to the ground due to the velocity difference between the freestream and the moving computational ground used in the present simulation. At $\Psi = 14^\circ$, surface streamlines on the GTS surface show the creation of two co-rotating vortices on the windward roof. For the present Ψ , similar flow structures between the two crosswind conditions are shown. Initial results show that the aerodynamic crosswind stability of a truck is related to the spanwise pressure difference between the windward and leeward surfaces of the truck.

Keywords: Truck aerodynamic; GTS; Crosswind stability; Overturn; Flow structure; Computational Fluid Dynamics (CFD).

NOMENCLATURE

A	GTS cross-section area	ε	turbulent dissipation rate
C_p	pressure coefficient	μ	dynamic viscosity
C_{pt}	total pressure coefficient	ρ	fluid density
C_r	rolling moment coefficient	τ	stress tensor
C_{sf}	side force coefficient	Ψ	GTS yaw angle
F	aerodynamic force	ω	specific turbulence dissipation rate
H	GTS height		
k	turbulent kinetic energy	Subscripts	
L	GTS length	CW	crosswind
M	aerodynamic moment	∞	freestream
p	static pressure	lee	leeward
pt	total pressure	R	roll
\mathbf{R}	vortical vorticity of a vortex	r	resultant
Re	Reynolds number	SF	side force
U	velocity	T	truck
\mathbf{u}	velocity vector	W	GTS width
W	GTS width	$wind$	windward
		2.5, 5, 7.5,	GTS yaw angles
		10, 14	
Greek Symbols			
β	crosswind incidence angle		

1. INTRODUCTION

An important subject in ground vehicle aerodynamics is crosswind stability. Ground vehicles, such as trucks, are more sensitive to crosswinds because of their larger side surfaces, increasing the side force acted on the truck, and therefore raising its rolling moment. Overturning caused 5% of fatal crashes involving large trucks in the United States between 2016 and 2018 (Baker *et al.* 2009). The most significant parameters to the crosswind stability are a combination of rolling moment coefficient (C_r) and load management (Federal Motor Carrier Safety Administration Analysis Division 2020).

Aerodynamic flow around the truck has similar characteristics to a flow around a bluff body. The aerodynamic characteristics of such flow are three-dimensional and massive flow separation due to an adverse pressure gradient in a streamwise direction. With the introduction of crosswind, fluid particles directly collide with the side of the truck generating a high-pressure region. Upon impact, some of the fluid particles move upward and some move downward. The flow separates on the roof corner of the truck and the underbody, generating additional low-pressure region.

The complexity of the flow around a detailed truck geometry has prompted researchers to develop diverse simplified geometries and study a distinct type of flow (Good and Garry 2004). Ground Transportation System (GTS) is one of the simplified truck geometries developed by NASA to study the GTS wake in an effort to reduce the aerodynamic drag. The GTS is a 1/8th scaled simplified Class 8 tractor/trailer configuration. It omits the tractor/trailer gap, side mirrors and detailed underbody (Fig. 1).

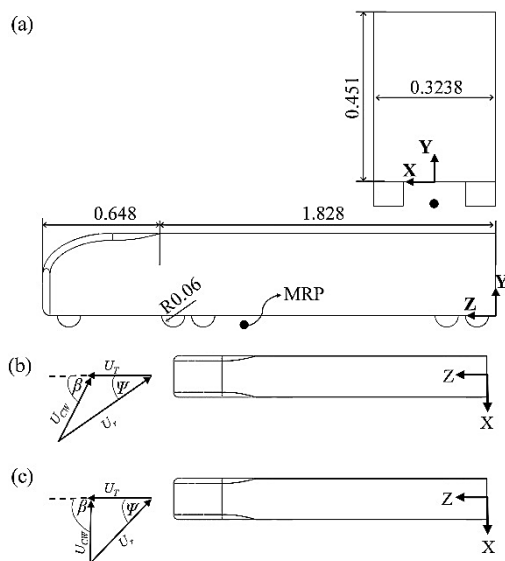


Fig. 1. (a) GTS dimensions (in meters), (b) definition of crosswind condition, (c) definition of pure crosswind condition.

The near-wake of the GTS at the symmetry plane for the turbulent Reynolds number ($Re_w \geq 1.6 \times 10^6$, where W is the GTS width) is defined by an upper, larger vortex feeding of the flow onto a lower vortex (Maddox *et al.* 2004; Roy and Ghuge 2009). At the GTS mid-height horizontal plane, the wake structure consists of a pair of counter-rotating vortex of equal size, merging onto one saddle point downstream (Salari *et al.* 2004; McArthur *et al.* 2016).

Croll *et al.* (1996) shows the creation of a pair of counter-rotating vortex on the upper edge of the GTS at yaw angle (Ψ) = 10° . These vortices travel downstream into the near wake region, breaking the symmetric vortices along the horizontal plane and shift the stagnation point on the base of the GTS (Van Raemdonck 2012). Pressure measurements by McArthur *et al.* (2018) on a detailed heavy vehicle show two low-pressure regions corresponds to the counter-rotating vortices near the roof of the GTS. Such vortices affect the crosswind stability of the vehicle (McArthur *et al.* 2018). Based on this observation, crosswinds appear to have a similar effect on the GTS, hence the GTS is an appropriate geometry for this study. Experiments by McArthur *et al.* (2013) show that the GTS achieves Re independence around $Re_w = 1.0 \times 10^6$, thus, it is expected that Re above this number will provide relevant insight into truck wakes at operational conditions.

Ψ is a function of truck speed (U_T), crosswind magnitude (U_{cw}) and incidence angle (β). When $\beta = 90^\circ$ (perpendicular to the truck side surface), the vehicle is under a *pure crosswind* condition. Figures 1 (b) and (c) shows definitions for *crosswind* and *pure crosswind*, respectively.

Computational Fluid Dynamics (CFD) simulations are integrated with automotive industries in parallel with experiments during the design process. Simulation offers more spatial freedom in the post-processing stage in comparison with experimental investigations. Large-Eddy Simulation (LES) is ideally used to accurately predict the flow around a ground vehicle. However, this method has a high computational cost, particularly at high Re (Rao *et al.* 2018). Because the present study focuses on the averaged flow condition around the GTS, the Reynolds-Averaged Navier-Stokes (RANS), which is less expensive than LES, is used rather than the LES. The RANS method has been widely used in the automotive industry (Bush *et al.* 2019).

In addition, RANS has been used in several studies to simulate a ground vehicle with and without crosswind. Dickison *et al.* (2020) utilize $k-\epsilon$ RANS model to develop a lightweight sport car. The wind tunnel tests validate the final design obtained from CFD. The drag and lift trend obtained from the wind tunnel tests can be predicted with the $k-\epsilon$ RANS (Dickison *et al.* 2020). Explicit Algebraic Stress Model (EASM) RANS based on $k-\omega$ Shear Stress Transport (SST) is used by Guilmineau and Chometon (2009) to study the aerodynamic properties of a simplified car model (Willy model) at $\Psi = 0^\circ-30^\circ$. The averaged aerodynamic coefficients, wall pressure, and total pressure at the wake area are

compared to experimental data and are able to capture the physics of crosswind flow (Guilmineau and Chometon 2009). Roy and Ghuge (2009) utilize $k-\omega$ SST RANS and Detached-Eddy Simulation (DES) to simulate the GTS at $\Psi = 0^\circ$. RANS and DES are able to obtain similar vortices formation at the wake area, and pressure distributions at the base of the GTS are within the experimental errors (Roy and Ghuge 2009). Hassaan *et al.* (2018) use $k-\omega$ SST RANS to simulate the GTS model at $\Psi = 0^\circ-15^\circ$. Under crosswind conditions, the RANS model could capture the asymmetry of the wake and mean flow properties around the GTS (Hassaan *et al.* 2018). The $k-\omega$ SST turbulence model is adopted in the present study as it offers a fairly accurate prediction of flow separation under an adverse pressure gradient (Menter 1994; Menter *et al.* 2003) and can capture the mean flow properties of the GTS with a crosswind condition (Hassaan *et al.* 2018).

The goals of this study are to investigate the flow structures of the GTS (near- and far-wake) and to determine which parameters are related to the crosswind stability of a truck from an aerodynamic standpoint. The physic of the longitudinal vortices on the roof of the GTS is discussed. The near-wake interactions downstream of the truck model are visualized and described. Initial result indicates that the side force and rolling moment of the GTS are related to the spanwise pressure difference between the windward and leeward surfaces. The work in this paper is the first step toward developing an overturn prevention device for a heavy vehicle. The remainder of the paper is organized in the following manner. Section 2 presents computational geometries, mesh topology, and numerical setup. Section 3 shows the validation study with the experimental data by Croll *et al.* (1996). Section 4 discusses the present numerical results by presenting flow structures at near- and far-wake of the GTS and plotting surface streamlines and pressure distribution on the GTS surface. Finally, conclusions are drawn in the last section.

2. NUMERICAL STRATEGY

The GTS key dimensions are shown in Fig. 1 (a). A positive Ψ defines a counter-clockwise rotation of the GTS relative to the Y axis about the Moment Reference Point (MRP). The MRP coordinates are defined at $[Z/L = 0.6, Y/H = -0.14, X/W = 0]$ and used by Croll *et al.* (1996) to measure the aerodynamic coefficients.

The side force (C_{sf}) and rolling moment (C_r) coefficients are determined at the MRP and the right-hand rule is used to determine the direction of the force and moment. The aerodynamic and non-dimensionalized coefficients are calculated using the following equations:

$$C_{sf} = \frac{F_{SF}}{0.5\rho U_\infty^2 A} \quad (1)$$

$$C_r = \frac{M_R}{0.5\rho U_\infty^2 AW} \quad (2)$$

$$C_p = \frac{(p - p_\infty)}{0.5\rho U_\infty^2} \quad (3)$$

$$C_{pt} = \frac{(pt - pt_\infty)}{0.5\rho U_\infty^2} \quad (4)$$

The numerical domain starts at $2 \times$ GTS length (L) from the leading edge of the GTS and extends to $7 \times L$ away from the trailing edge of the GTS. The height of the domain is $6.6 \times H$, and its width is $31 \times W$ (Fig. 2), which gives a blockage ratio of $\sim 0.6\%$. The GTS wheels are position above the computational ground with a clearance of $0.04 \times W$ (Croll *et al.* 1996). Figure 2 presents the computational domain and its size.

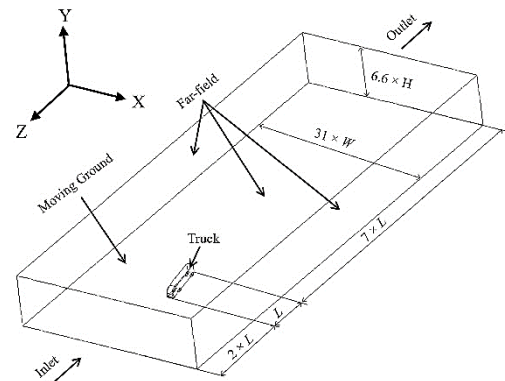


Fig. 2. Computational domain and boundary conditions applied to the surfaces.

Flow passing through a ground vehicle can be assumed as an incompressible flow. Therefore, the governing equations are:

$$\nabla \cdot \mathbf{u} = 0 \quad (5)$$

$$\frac{\partial \mathbf{u}}{\partial t} + \nabla \cdot (\mathbf{u} \times \mathbf{u}) = -\frac{1}{\rho} \nabla p + \nabla \cdot \boldsymbol{\tau} \quad (6)$$

The ANSYS® CFX code is used to conduct the CFD simulations. Turbulence is modeled with a two-equations turbulence model, $k-\omega$ SST by Menter *et al.* (2003). The $k-\omega$ SST is a hybrid between $k-\epsilon$ in the freestream and $k-\omega$ inside the near-wall region. Formulation of the $k-\omega$ SST are given below and detailed derivations of such model can be seen in Menter (1994) and Menter *et al.* (2003).

$$\frac{\partial(\rho k)}{\partial t} + \frac{\partial(\rho U_i k)}{\partial x_i} = P_k - \theta^* \rho k \omega + \dots$$

$$\frac{\partial}{\partial x_i} \left[(\mu + \sigma_k \mu_t) \frac{\partial k}{\partial x_i} \right] \quad (7)$$

$$\frac{\partial(\rho \omega)}{\partial t} + \frac{\partial(\rho U_i \omega)}{\partial x_i} = \alpha \rho S^2 - \theta \rho \omega^2 + \dots$$

$$\frac{\partial}{\partial x_i} \left[(\mu + \sigma_\omega \mu_t) \frac{\partial \omega}{\partial x_i} \right] + \dots$$

$$2(1 - F_1) \rho \sigma_{\omega^2} \frac{1}{\omega} \frac{\partial k}{\partial x_i} \frac{\partial \omega}{\partial x_i} \quad (8)$$

$$v_t = \frac{a_1 k}{\max(a_1 \omega, SF_2)} \quad (9)$$

$$P_k = \mu_t \frac{\partial U_i}{\partial x_j} \left(\frac{\partial U_i}{\partial x_j} + \frac{\partial U_j}{\partial x_i} \right) \quad (10)$$

The ANSYS® CFX code employs a vertex-based finite volume method to discretize the governing equations. The ANSYS® CFX uses a co-located grid layout which allows the control volumes to be identical for all transport equations. Rhie *et al.* (1983) proposed an alternative discretization to avoid pressure-field decoupling, which was further modified by Majumdar (1988) to provide timestep independence of a steady-state solution. The solver uses a pseudo-transient approach to accelerate a solution in reaching a steady-state, which means the timestep acts as an acceleration parameter. Algebraic Multigrid (Raw 1996) is implemented inside the code to enhance the solver performances in solving a discrete system of linearized equations.

The boundary conditions applied for solving the CFD simulations are defined below (shown in Fig. 2):

- Inlet velocity (U_∞) = 76.35 m/s with a 0.25% turbulence intensity is applied at the inlet boundary for *crosswind* conditions. CFD simulations are performed for $\Psi = 0^\circ-14^\circ$, as suggested by Hucho and Sovran (1987). On *pure crosswind* conditions, U_∞ is the resultant velocity (U_r) of U_T (76.35 m/s) with U_{cw} and defined in Eq. (12). The working fluid is air at 25°C.

$$Re_w = \frac{\rho U_\infty W}{\mu} \quad (11)$$

$$U_r = \frac{U_T}{\cos(\Psi)} \quad (12)$$

- A static pressure equals to 101,325 Pa is imposed at the outlet boundary. A free-slip wall is assigned as a boundary condition for far-field surfaces, while the truck surfaces have a non-slip wall boundary. A non-slip wall with a velocity equal to U_T in the negative Z direction is applied at the ground surface.

At each iteration, the advection and turbulence terms are approximated using the high-resolution discretization scheme proposed by Barth and Jespersen (1989). The pseudo-transient timestep is set to be equal to 2.0×10^4 s. Three convergence criteria are considered; the momentum and continuity residuals must be below 10^{-3} , imbalances in the computational domain have to be below 0.01, and the variation of the Cr and Csf is less than 0.01.

The computational mesh consists of triangular mesh on the computational surfaces and a combination of tetrahedral and prism meshes on the computational volume. 20 prism layers are extruded on the truck and ground surfaces and the average y^+ is kept ~ 1 . Figure 3 shows the y^+ distribution on the GTS body. Except for the fillet surfaces with a high velocity gradient, the majority of the GTS surfaces have y^+ values less than 1. Meshes with smaller sizes are generated near the GTS body to capture the flow physics. To ensure a high-quality mesh, the aspect ratio of the computational meshes is greater than 0.2. Figure 4 presents the computational mesh generated with the ANSYS® ICEM CFD.

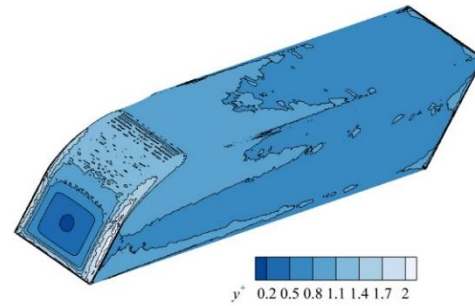


Fig. 3. y^+ distribution on the GTS body.

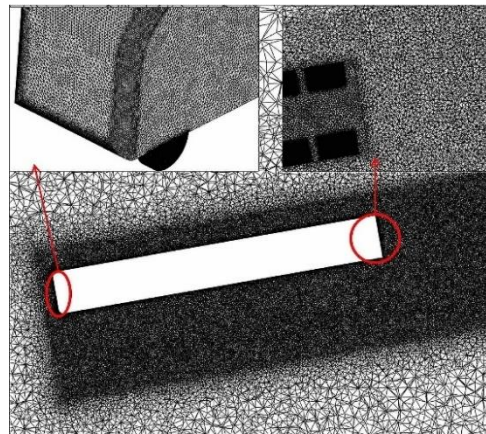


Fig. 4. Top view of the computational mesh used in the study for $\Psi = 10^\circ$. (Left inset) an overview of the surface mesh. (Right inset) Closer look to the volume mesh near the GTS.

A mesh independence study is done with four cases with a total number of grids ranging from $\sim 9.0 \times 10^6$ to $\sim 21.0 \times 10^6$. Table 1 shows the mesh independence study performed at $\Psi = 10^\circ$. It can be observed that the variation of Cr and Csf between case 3 (16.1×10^6) and case 4 (21.1×10^6) is less than 1%, hence, mesh topology similar to case 3 is chosen.

Table 1 Grid independence study. Discrepancy is compared with the chosen mesh (16,063,112)

Mesh elements	Cr	Cr discrepancy (%)	Csf	Csf discrepancy (%)
9,113,325	-1.0682	2.7	1.415	2.7
10,964,063	-1.0739	2.2	1.397	1.4
16,063,112	-1.0981	-	1.3778	-
21,148,800	-1.1024	-0.4	1.37	-0.5

Vortex structures have to be extracted from the flow field to investigate their nature. The most commonly used methods are Q -criterion (Hunt *et al.* 1989), λ_2 -criterion (Jeong and Hussain 1995), and a more recent Ω method (Liu *et al.* 2016). This study uses the Ω method to extract vortex structures. The Ω method is based on the Helmholtz fluid velocity decomposition. Ω represent the ratio of vorticity square over the summation of vorticity square and deformation square (defined in Eq. (13)). It has a clear physical meaning, which is that a vortex exists when the rotation is larger than deformation ($\Omega > 0.5$) (Liu *et al.* 2016). The vortex visualization is based on the idea in which the vortical vorticity is related to vortex motions. Liu *et al.* (2016) recommend a threshold value of $\Omega = 0.52$ to define vortex motions as it is a good quantity to capture vortices due to flow separations and transitions.

$$\Omega = \frac{(\nabla \times \mathbf{u} \cdot \mathbf{R})^2}{\|\nabla \times \mathbf{u}\|_2^2 \cdot \|\mathbf{R}\|_2^2} \quad (13)$$

3. VALIDATION

Figures 5 (a) and (b) presents validation results of the C_r and C_{sf} calculated in the presents CFD simulations with the experimental results of Croll *et al.* (1996). Both aerodynamic coefficients computed in this study agree reasonably well with the experimental results (Croll *et al.* 1996). In addition, pressure coefficient (C_p) comparisons at $Y/W = 0.7$ is presented in Fig. 5 (c). The numerical result predicts a similar C_p trend with the experimental data by Croll *et al.* (1996), despite lower values on both the windward and leeward sides.

The moving ground boundary condition applied in this study results in a thinner boundary layer on the ground, relative to the stationary ground used by Croll *et al.* (1996). With a ground clearance of $0.04 \times W$ between the wheels and the ground, a thicker boundary layer on the ground during the experiment may interact with the boundary layer developed on the GTS. The difference in the ground boundary condition leads to a higher C_p value on the base of the GTS, predicted by the CFD. Garry (1996) made the same observation during his experiment on a bluff body with moving ground conditions.

4. RESULTS AND DISCUSSIONS

The following section discusses the effect of Ψ variations and crosswind conditions (*crosswind* and *pure crosswind*) on the GTS flow structures at near- and far-wake areas. Section 4.2 presents surfaces streamlines and C_p contours on the GTS surface, furthermore, the relation between spanwise pressure difference with C_r and C_{sf} is shown.

4.1 Flow Structures

Figure 6 presents iso-surface contours of $\Omega = 0.52$ around the GTS to visualize vortex structures for $\Psi = 0^\circ, 7.5^\circ$, and 14° . The near-wake structure for GTS without crosswind ($\Psi = 0^\circ$) consists of a pair of counter-rotating vortex (labeled A and B). Upper

(A*), lower (B*) and sides (C* and D*) shear layers separate at the base due to an adverse pressure gradient. Additional two symmetric streamwise vortices take birth from the upstream wheels of the GTS.

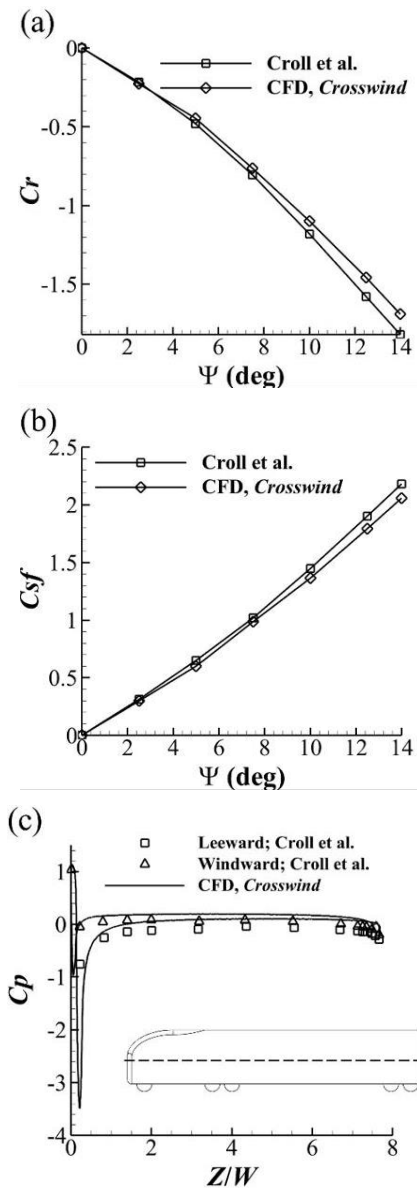


Fig. 5. Comparisons of the present CFD with the experimental work by Croll *et al.* (1996); (a) C_r , (b) C_{sf} , and (c) C_p at $Y/W = 0.7$ (dashed line in the inset) for $\Psi = 10^\circ$.

The definite alteration in the flow field near the GTS with Ψ , relative to $\Psi = 0^\circ$, is the emergence of two longitudinal vortices originating from the roof ϵ and leeward sides of the GTS (F), due to separation on the sharp corner on the roof.

The effect of Vortices E and F can be seen for $\Psi = 7.5^\circ$ and 14° . Downstream of the GTS, the interaction between the counter-rotating Vortices A and B with a clockwise rotating Vortex E induces a downward shift of the tip of Vortex E (labeled J).

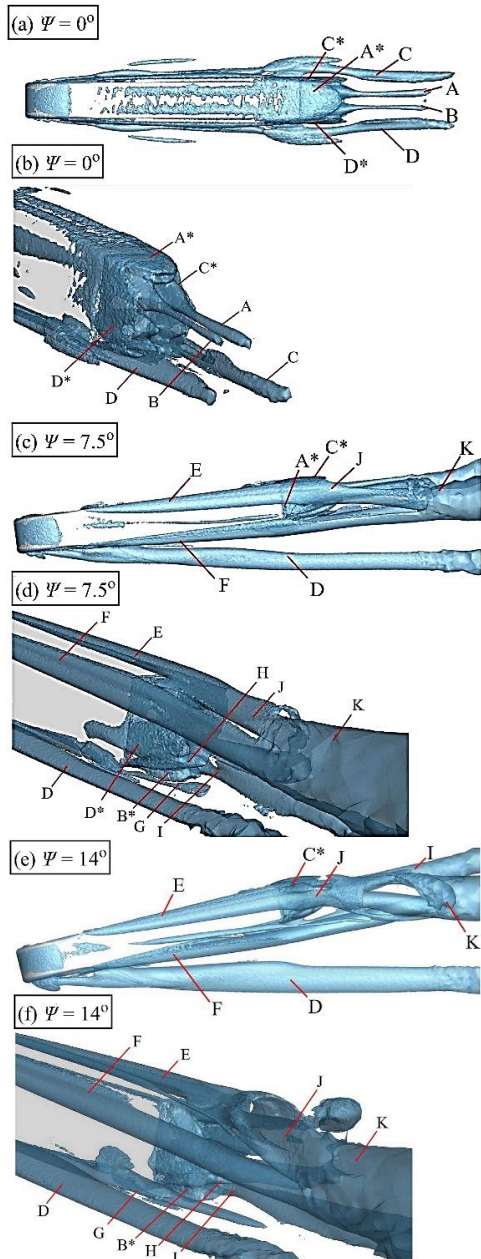


Fig. 6. Visualization of $\Omega = 0.52$ iso-surfaces near the GTS; (a) and (b) 0° , (c) and (d) 7.5° , (e) and (f) 14° .

Vortices F and J then interact with Vortices A and B, which leads to size shrinkage of Vortices A and B. The crosswind pushes the axes of Vortices E and F in the crossflow direction. The tip of Vortex E shifts downward (J), while Vortex F advances to the leeward side, propagating away from the GTS body. Further downstream, Vortex J along with Vortex F merge into one longitudinal vortex (K).

The iso-surface contours suggest that the size of Vortices E and F is increased with an increase of Ψ . For $\Psi > 0^\circ$, the pressure difference between the windward and leeward sides, invokes shear layer separation at the upper edge of the windward side of the GTS. As the vortices travel downstream toward the wake area, diffusion of vorticity dominates and gives rise to the axial pressure (Lambourne and

Bryer 1961). An enlargement of the vortex core due to diffusion (Helmholtz theorem of vorticity) results in a decrease in rotational velocity (to maintain a constant circulation), which enhances the pressure rise (Lambourne and Bryer 1961). The pressure rise is accompanied by the deceleration of the axial velocity, and according to Kelvin's Circulation Theorem, velocity deceleration is related to the growth of vortex size. Such mechanism is also responsible for Vortex F at the leeward upper edge.

Note that the trajectory and size of Vortices C and D have similar characteristics with Vortices E and F. From flow visualization, the crosswind further drives the trajectory of Vortex D to the leeward side, therefore, has a minimal influence on the near-wake structure. On the other hand, Vortex C seems to merged with the lower shear layer (B^*). As a result, the lower vortex has a bigger strength compared to its counterpart and pull Vortex J towards the ground.

The presence of the wheels near the base of the GTS generates Vortices G and I at the ground level for all Ψ . Downstream of the GTS with Ψ , vortices generated by the wheels propel upward (H) due to an upwash motion from the underbody flow.

Figures 7 and 8 shows the total pressure coefficient (C_{pt}) contours downstream of the GTS under a crosswind condition at $\Psi = 7.5^\circ$ and 14° , respectively. Near the GTS base ($Z/W = 0$), two isolated low total pressure regions can be seen on the roof (Vortex E) and leeward side (F). At the ground level of the leeward side, two additional total pressure cores generated by the upstream wheels (D and G) can be observed. For $\Psi = 14^\circ$, Vortex F detaches from the GTS main body, relative to $\Psi = 7.5^\circ$.

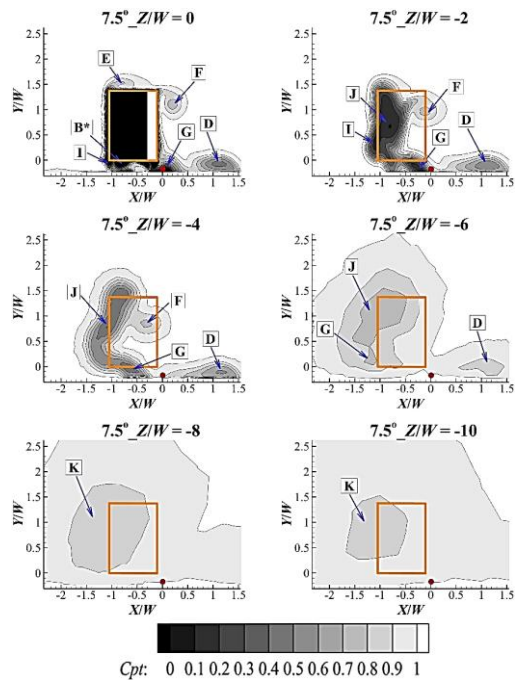


Fig. 7. C_{pt} contours for $\Psi = 7.5^\circ$ under crosswind. Orange lines represent the GTS base region. Red dot is the MRP.

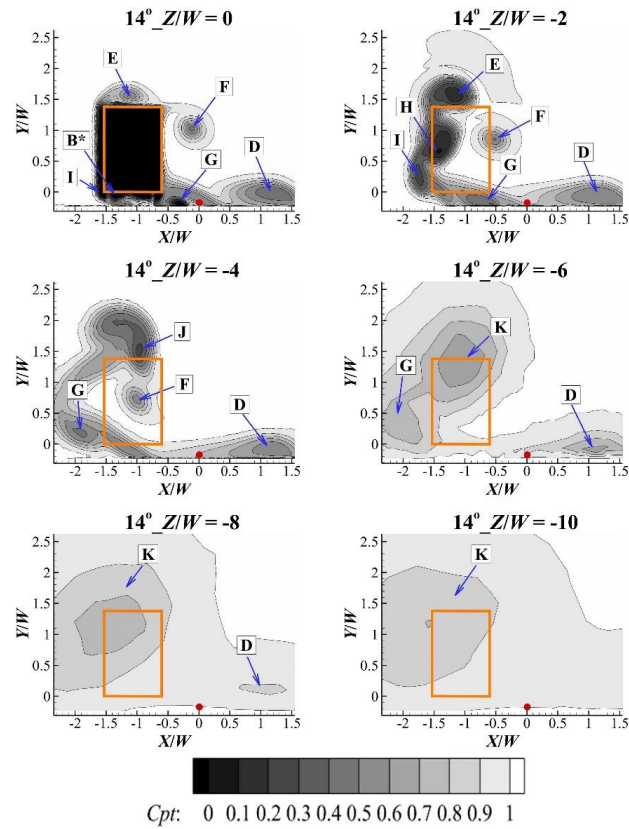


Fig. 8. C_{pt} contours for $\Psi = 14^\circ$ under crosswind. Orange lines represent the GTS base region. Red dot is the MRP.

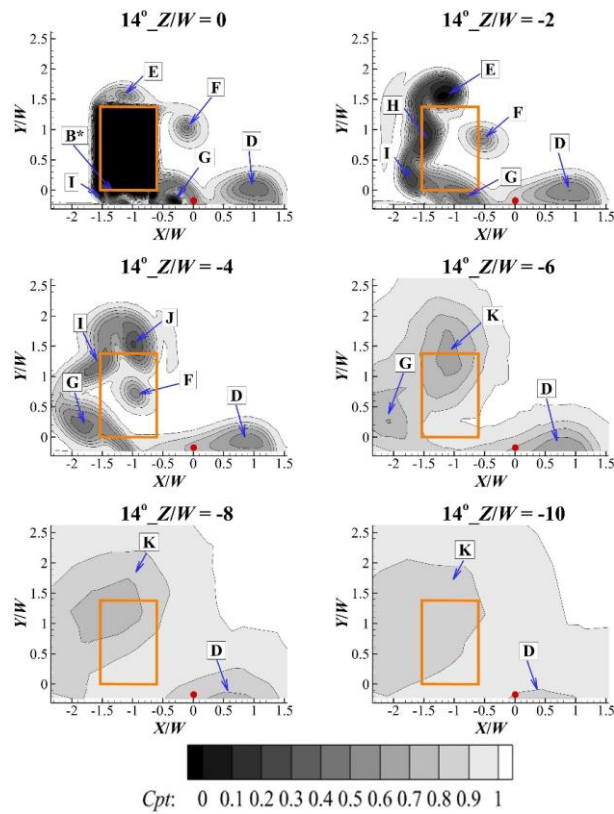


Fig. 9. C_{pt} contours for $\Psi = 14^\circ$ under pure crosswind. Orange lines represent the GTS base region. Red dot is the MRP.

At $Z/W = -2$, the trajectory of Vortices E and F begin to tilt both inwards and downwards, approaches the center of the GTS. The same observation has been made by an experimental work of [McArthur et al. \(2018\)](#) for a detailed heavy vehicle at $Re_w = 1.4 \times 10^6$. The bulk of the wake structure moves in a similar pattern as mentioned before.

The emergence of Vortex K (as a result of the combination between the tip of Vortices E and F) takes place from $Z/W > -4$ ($\sim 0.5 \times L$) for both Ψ . At $Z/W = -4$, the core of Vortex G separates from the ground and is absorbed by Vortex K at $Z/W > -6$. This core continues to travel downstream of the GTS and continues to propagate downstream while regaining its energy and dissipates from $Z/W > -6$ and $Z/W > -8$ for $\Psi = 7.5^\circ$ and 14° , respectively.

The size and intensity of the vortex cores increase as Ψ increases. As a result, the inner low total pressure core at the far-wake of higher Ψ may travel a greater distance before dissipating.

Figure 9 shows the C_{pt} contours of the wake at $\Psi = 14^\circ$ under a *pure crosswind* as it progresses downstream. It should be noted that $\Psi = 14^\circ$ is chosen for visualization to highlight the variation of the structure. The wake characteristics for the *pure crosswind* condition are identical with the *crosswind* condition, but with a slightly higher magnitude. Due to the difference in velocity between the freestream and the moving ground, the inner low total pressure core for the *pure crosswind* condition advances toward the ground and remains.

4.2 Wall pressure, surface streamlines, and aerodynamic coefficients

Figures 10 and 11 present surface streamlines and C_p contours on the GTS surface under *crosswind* conditions for $\Psi = 7.5^\circ$ and 14° , respectively. The streamlines patterns in these figures are comprised of the following main elements:

- 1) *Front attachment point.* Fluid particles firstly hit the GTS front surface at the front attachment point, creating a stagnation pressure nearby. As Ψ increases, the front attachment point shifts toward the windward side. Fluid particles then spread out from this point.
- 2) *Windward separation and outer windward separation.* Fluid particles from the windward surface of the GTS separate at the upper edge creating a roll-up vortex (Vortex E). The location where these separation lines form is shifted upstream with the increase of Ψ .
- 3) *Windward and outer windward re-attachment.* At this line, the vortex correlated with the windward and outer windward separation re-attaches on the roof surface. Fanning out of the re-attachment line is a corollary to the detachment of the inner windward separation vortex from the roof.
- 4) *Inner windward separation.* Nearby the outer windward re-attachment line, the flow separates

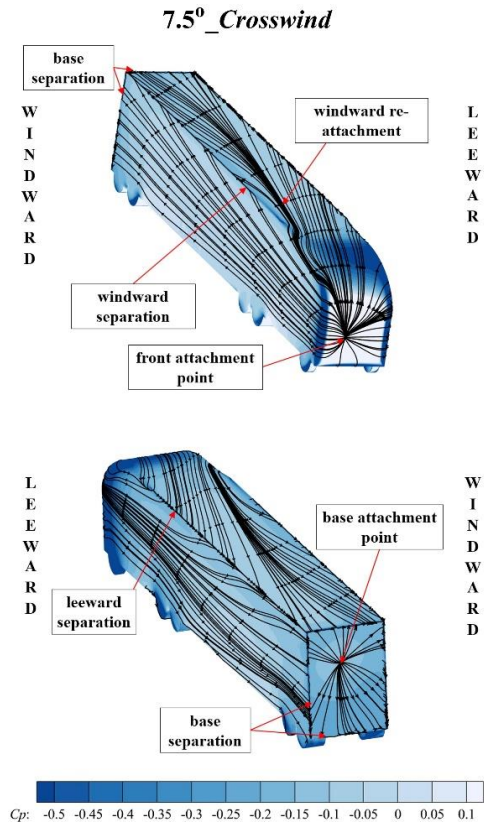


Fig. 10. Surface streamlines on the GTS surface at $\Psi = 7.5^\circ$ flooded with C_p contours.

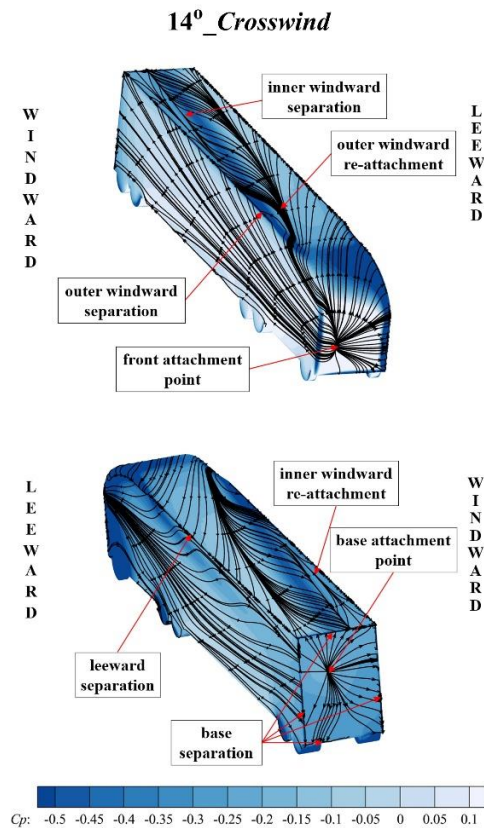


Fig. 11. Surface streamlines on the GTS surface at $\Psi = 14^\circ$ flooded with C_p contours.

for the second time, forming a vortex with a smaller magnitude.

- 5) *Inner windward re-attachment.* The vortical flow correlated with the inner windward separation re-attaches along this line. The flow then travels until it arrives at the outer windward separation line, where it separates and re-circulates to the outer windward re-attachment line.
- 6) *Leeward separation.* After the flow re-attached as described in element 5, the flow travels to the leeward edge and separates, thus the leeward vortex takes birth along this line (Vortex F). This line forms earlier as Ψ increases. For $\Psi = 7.5^\circ$ and 14° , the separation line forms at the leeward edge and leeward radii, respectively.
- 7) *Base separation.* The separation and re-attachment lines mentioned on element 2-6 extend to the base of the GTS, where they separate at the edges (Vortices A*, B*, C*, D*).
- 8) *Base attachment point.* At this point, the near-wake re-attaches and creates a stagnation

pressure on the base surface.

The notable alteration in the surface streamlines, observed for $\Psi = 14^\circ$, relative to $\Psi = 7.5^\circ$, is the emergence of the outer/inner windward separation/re-attachment lines, indicating two co-rotating vortices at the windward roof which are not visible in Fig. 5.

From the C_p contours on the GTS surface in Figs. 10 and 11, an increase in Ψ causes an increase in pressure at the windward surface and a decrease in pressure at the roof and leeward surfaces. Therefore, the pressure difference between the windward and leeward surfaces is higher with an increasing Ψ . At the base of the GTS, the stagnation pressure shifts to the upper leeward half of the surface, due to an influence of the roof vortices (Vortices E and F) (Hassaan *et al.* 2018). In addition, low-pressure regions at the lower half of the base become more dominant as Ψ increases, as a result of the upwash motion from the underbody flow. Noted that the flow physics for *crosswind* and *pure crosswind* are similar, hence visualization only considers *crosswind* conditions.

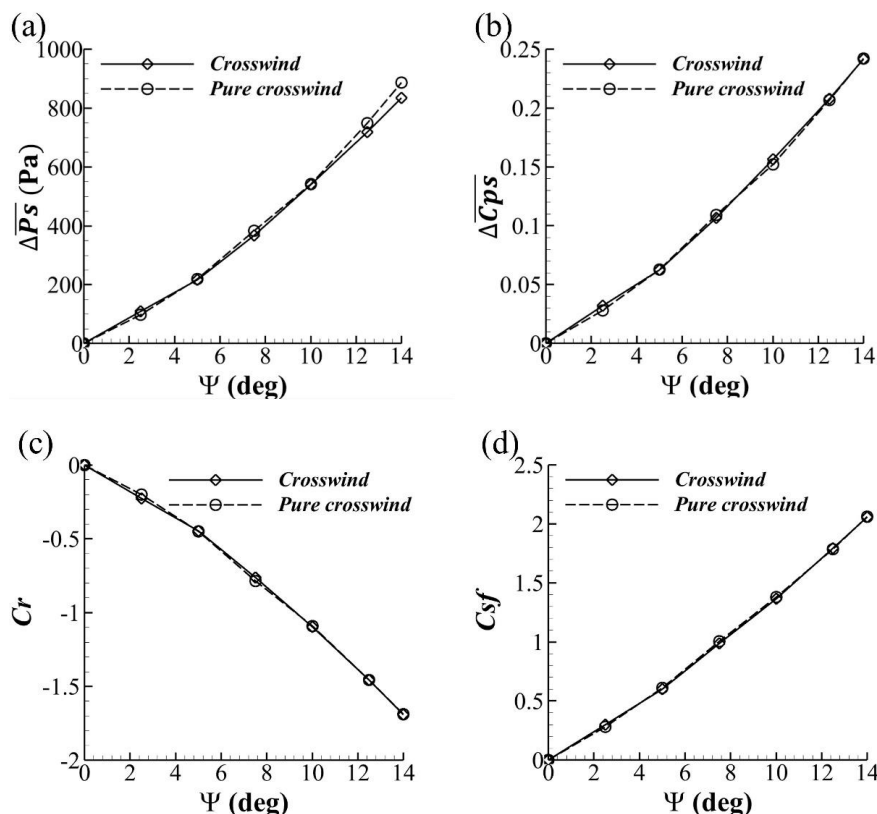


Fig. 12. Comparisons between *crosswind* and *pure crosswind*; (a) $\overline{\Delta P_s}$, (b) $\overline{\Delta C_{ps}}$, (c) C_r and (d) C_{sf} .

Figure 12 (a) presents the mean spanwise pressure difference between the windward and leeward side ($\overline{\Delta P_s}$, defined in Eq. (14)). A nearly linear rise in $\overline{\Delta P_s}$ relative to Ψ can be seen for both *crosswind* and *pure crosswind*. The effect of β is more visible as Ψ increases, with a larger value in $\overline{\Delta P_s}$ for the *pure crosswind* as expected. However, the mean spanwise

C_p difference ($\overline{\Delta C_{ps}}$, defined in Eq. (15)) shows slight variations between *crosswind* and *pure crosswind* conditions (Fig. 12 (b)). As Ψ increases, magnitudes for both U_∞ and freestream dynamic pressure also increase for the *pure crosswind*. This suggests that pressure losses in the flow field due to the kinetic energy is more dominant, relative to the

pressure gains experienced by the GTS, for the *pure crosswind*.

$$\overline{\Delta P_s} = \overline{P_{wind}} - \overline{P_{lee}} \quad (14)$$

$$\overline{\Delta C_{ps}} = \overline{C_{p_{wind}}} - \overline{C_{p_{lee}}} \quad (15)$$

The Cr and Csf values for both *crosswind* and *pure crosswind* are shown in Figs. 12 (c) and (d), respectively. Since the Cr and Csf are directly related to the dynamic pressure, bot values (in magnitude) for the *crosswind* and *pure crosswind* increase as Ψ increases, the same progressions as the $\overline{\Delta C_{ps}}$. The above discussions suggest that the Cr and Csf of the GTS are related to the spanwise pressure difference.

5. CONCLUSIONS

This paper presents numerical simulations on a simplified truck model called the GTS with $\Psi = 0^\circ$ - 14° . Simulations are performed using the steady $k-\omega$ SST RANS turbulence model. Cr , Csf , and Cp distributions on the GTS are compared with the experimental results by Croll *et al.* (1996). In general, the Cr , Csf , and Cp predicted by the CFD are in a good agreement with the experimental data. Comparisons of the flow visualizations obtained from the current CFD and literature (Hassaan *et al.* 2018; McArthur *et al.* 2016) suggest that the current CFD could capture the three-dimensional asymmetric flow structure of the GTS.

On the introduction of Ψ , a substantial change in the flow structure is observed. Such change is the emanation of the vortices on the roof originating at its windward/leeward edges and underbody vortices forming due to the presence of the wheels. Vortices on the roof grow in size as they move downstream. The growth in size is related to the pressure rise inside their cores. Such pressure rise is followed by the decline in the axial velocity, hence size growth (Kelvin's Circulation Theorem). The roof vortices continue to develop downstream of the GTS, where they interact and merge into on longitudinal vortex. The merging process happened at $Z/W > -4$ for $\Psi = 7.5^\circ$ and 14° . The merged core continues to propagate downstream until it dissipates at $Z/W > -6$ and $Z/W > -8$ for $\Psi = 7.5^\circ$ and 14° , respectively. For the *pure crosswind* condition, the merged vortex attaches to the ground due to the velocity differences between the freestream and the moving ground. From the surface streamlines visualization, two co-rotating vortices are observed on the windward roof of the GTS for $\Psi = 14^\circ$. In general, a similar flow structure is observed for *crosswind* and *pure crosswind* conditions. This is due to the low Ψ chosen in the present study.

This paper is a first step for which the final goal is to develop an overturn prevention device for a truck. Comparisons between the spanwise pressure difference with Cr and Csf , suggest that the aerodynamic crosswind stability of a truck is related to such pressure difference and can be improved by lowering its value.

ACKNOWLEDGEMENTS

The authors would like to thank Jetpro Technology Inc. for sponsorship of this research.

REFERENCES

- Baker, C. J., F. Cheli, A. Orellano, N. Paradot, C. Proppe and D. Rocchi (2009). Cross-wind effects on road and rail vehicles. *Journal of Wind Engineering and Industrial Aerodynamics* 47, 983-1022.
- Barth, T. and D. Jespersen (1989, January). The design and application of upwind schemes on unstructured meshes. In *27th Aerospace Sciences Meeting*, Nevada, USA.
- Bush, R. H., T. Chyczewski, K. Duraisamy, B. Eisfeld, C. L. Rumsey and B. R. Smith (2019, January). Recommendations for future efforts in RANS modeling and simulation. In *AIAA Scitech 2019 Forum*, California, USA.
- Croll, R. H., W. T. Gutierrez, B. Hassan, J. E. Suazo and A. J. Riggins (1996). Experimental investigation of the ground transportation system (GTS) project for heavy vehicle drag reduction. *SAE Technical Paper* 960907.
- Dickison, M., M. Ghaleeh, S. Milady, S. Subbakrishna, L. T. Wen and M. A. Qubeissi (2020). Investigation into the Aerodynamic Performance of a Concept Sports Car. *Journal of Applied Fluid Mechanics* 13(2), 583-601.
- Federal Motor Carrier Safety Administration Analysis Division (2020). *Large Truck and Bus Crash Facts 2018*. Report, U.S. Department of Transportation, FMCSA-RRA-19-018.
- Garry, K. P. (1996). Some effects of ground clearance and ground plane boundary layer thickness on the mean base pressure of a bluff body vehicle type body. *Journal of Wind Engineering and Industrial Aerodynamics* 62, 1-10.
- Good, G. M. L. and K. P. Garry (2004). On the use of reference models in automotive aerodynamics. *SAE Technical Paper* 2004-01-1308.
- Guilmineau, E. and F. Chometon (2009). Effect of side wind on a simplified car model: experimental and numerical analysis. *Journal of Fluids Engineering* 131, 021104.
- Hassaan, M., D. Badlani and M. Nazarinia (2018). On the effect of boat-tails on a simplified heavy vehicle geometry under crosswinds. *Journal of Wind Engineering and Industrial Aerodynamics* 183, 172-186.
- Hucho, W. H. and G. Sovran (1987). *Aerodynamics of Road Vehicles: from Fluid Mechanics to Vehicle Engineering*. Cambridge, UK.
- Hunt, J. C. R., A. A. Wray and P. Moin (1988). *Eddies, stream and convergence zones in*

- turbulent flows*. Report, NASA, N89-24555. 364-375.
- Jeong, J. and F. Hussain (1995). On the identification of a vortex. *Journal of Fluid Mechanics* 285, 69-94.
- Lambourne, N. C. and D. W. Bryer (1961). *The bursting of leading-edge vortices-some observation and discussion of the phenomenon*. Report, National Physical Laboratory, 3282.
- Liu, C. Q., Y. Q. Wang, Y. Yang and Z. W. Duan (2016). New omega vortex identification method. *Science China Physics, Mechanics & Astronomy* 59.
- Maddox, S., K. D. Squires, K. E. Wurtzler and J. R. Forsythe (2004). Detached-eddy simulation of the ground transportation system. In R. McCallen *et al.* (Eds.), *The Aerodynamics of Heavy Vehicles II: Trucks, Buses, and Train*, Berlin, 19, 89-104. Springer.
- Majumdar, S. (1988). Role of underrelaxation in momentum interpolation for calculation of flow with nonstaggered grids. *Numerical Heat Transfer* 13, 125-132.
- McArthur, D., D. Burton, M. Thompson and J. Sheridan (2013). Development of a wind tunnel section for evaluation of heavy vehicle aerodynamic drag at a scale of 1:3. *SAE International Journal of Commercial Vehicles* 6, 522-528.
- McArthur, D., D. Burton, M. Thompson and J. Sheridan (2016). On the near wake of a simplified heavy vehicle. *Journal of Fluids and Structures* 66, 293-314.
- McArthur, D., D. Burton, M. Thompson and J. Sheridan (2018). An experimental characterization of the wake of a detailed heavy vehicle in cross-wind. *Journal of Wind Engineering and Industrial Aerodynamics* 175, 364-375.
- Menter, F. R. (1994). Two-equation eddy-viscosity turbulence models for engineering applications. *AIAA Journal* 32, 1598-1605.
- Menter, F. R., M. Kuntz and R. Langtry (2003). Ten years of industrial experience with the sst turbulence model. *Turbulence, Heat and Mass Transfer* 4.
- Rao, A. N., J. Zhang, G. Minelli, B. Basara and S. Krajnovic (2018). An LES investigation of the near-wake flow topology of a simplified heavy vehicle. *Flow, Turbulence and Combustion* 102, 389-415.
- Raw, M. J. (1996, January). Robustness of coupled algebraic multigrid for the navier-stokes equations. In *34th Aerospace Sciences Meeting and Exhibit*, Nevada, USA.
- Rhie, C. M. and W. L. Chow (1983). A numerical study of the trubulent flow past an isolated airfoil with trailing edge separation. *AIAA Journal* 21, 1525-1532.
- Roy, C. J. and H. A. Ghuge (2009). Detached-eddy simulations of a simplified tractor/trailer geometry. In R. McCallen *et al.* (Eds.), *The Aerodynamics of Heavy Vehicles II: Trucks, Buses, and Train*, Berlin, 41, 363-381. Springer.
- Salari, K., J. Ortega and P. Castellucci (2004, June). Computational prediction of aerodynamic forces for a simplified integrated tractor-trailer geometry. In *34th AIAA Fluid Dynamics Conference and Exhibit*, Oregon, USA.
- Van Raemdonck, G. M. R. (2012). *Design of low drag bluff road vehicles*. Ph. D. thesis, Delft University of Technology, Delft, Netherlands.